nature nanotechnology

LETTERS

PUBLISHED ONLINE: 9 MARCH 2014 | DOI: 10.1038/NNANO.2014.25

Optoelectronic devices based on electrically tunable p–n diodes in a monolayer dichalcogenide

Britton W. H. Baugher†, Hugh O. H. Churchill†, Yafang Yang and Pablo Jarillo-Herrero*

The p–n junction is the functional element of many electronic and optoelectronic devices, including diodes, bipolar transistors, photodetectors, light-emitting diodes and solar cells. In conventional p–n junctions, the adjacent p- and n-type regions of a semiconductor are formed by chemical doping. Ambipolar semiconductors, such as carbon nanotubes[1], nanowires[2] and organic molecules[3], allow for p–n junctions to be configured and modified by electrostatic gating. This electrical control enables a single device to have multiple functionalities. Here, we report ambipolar monolayer WSe_2 devices in which two local gates are used to define a p–n junction within the WSe_2 sheet. With these electrically tunable p–n junctions, we demonstrate both p–n and n–p diodes with ideality factors better than 2. Under optical excitation, the diodes demonstrate a photodetection responsivity of 210 mA W^{-1} and photovoltaic power generation with a peak external quantum efficiency of 0.2%, promising values for a nearly transparent monolayer material in a lateral device geometry. Finally, we demonstrate a light-emitting diode based on monolayer WSe_2. These devices provide a building block for ultrathin, flexible and nearly transparent optoelectronic and electronic applications based on ambipolar dichalcogenide materials.

Next-generation photodetectors and photovoltaic devices, as well as sensors, displays and light-emitting diodes, will require new optoelectronic materials with characteristics superior to those currently in use. Candidate materials must be flexible for wearable devices, transparent for interactive displays, efficient for solar cells and robust for broad distribution. Monolayer semiconducting transition-metal dichalcogenides (TMDs) such as tungsten diselenide (WSe_2) are flexible[4], nearly transparent[5–7], high-strength[4] and direct-bandgap[5] materials with the potential to meet all of these criteria. The crystal structure of WSe_2 comprises stacks of sheets, each made of one atomic layer of tungsten encapsulated by two layers of selenium. This structure leads to strong intralayer and weak interlayer bonding[4], allowing the exfoliation of bulk crystals down to a single Se–W–Se layer, similar to graphene.

Monolayer WSe_2 is a direct-gap semiconductor with a bandgap of ~1.65 eV (ref. 8), and is therefore a complement to other two-dimensional materials[9] such as graphene, a gapless semimetal, and boron nitride, an insulator. The direct bandgap distinguishes monolayer WSe_2 from its bulk and bilayer counterparts, which are both indirect gap materials with smaller bandgaps[8,10]. This sizable direct bandgap in a two-dimensional layered material enables a host of new optical and electronic devices. Thin-film TMDs have already been used in the demonstration of novel nanoelectronic and optoelectronic devices such as ambipolar and high-quality field-effect transistors[11,12], electric double-layer transistors[13], integrated circuits[14] and phototransistors[15] with high responsivity[16]. In addition, photoluminescence[5] and electroluminescence[17,18] have revealed effects including giant spin-valley coupling[19] and optical control of valley polarization[20,21] and coherence[22].

To date, p–n junctions in TMDs have been explored less than field-effect transistors. Junctions of p- and n-doped bulk WSe_2 were reported over 30 years ago[23]. More recently, p–n devices have been constructed of low-dimensional semiconductors[24] and thin-film TMDs, such as an ionic-liquid gated bulk MoS_2 device[13], an InAs/bulk WSe_2 heterojunction[6] and a doped silicon/-monolayer MoS_2 heterojunction[18]. Unfortunately, bulk TMDs and heterostructures involving other materials lack many of the most appealing properties of monolayer TMDs, such as direct bandgap, flexibility and transparency. Here, we characterize monolayer WSe_2 p–n junctions defined and controlled by electrostatic gates, demonstrating devices with diverse functionality, including current-rectifying diodes, a photodetector, a photovoltaic device and a light-emitting diode.

Device fabrication made use of exfoliated natural crystals of WSe_2, with monolayer flakes transferred[25] onto substrates with a prepatterned pair of local backgates separated by 100 nm and covered by 20 nm of HfO_2. An optical image and schematic of the device used for all measurements except electroluminescence are presented in Fig. 1a. Comprehensive fabrication details are provided in the Methods and the Supplementary Information. All measurements were performed at room temperature and in vacuum (~10^{-5} torr), with a voltage bias V_{ds} applied to the source contact and the direct current through the device, I_{ds}, measured at the drain.

The voltages on the two gates (V_{lg} for the left gate and V_{rg} for the right gate) independently control the carrier density in the left and right sides of the monolayer. In this way, the device can be electrostatically doped into various conducting regimes (Fig. 1). With both sides of the device n-doped ($V_{lg} = V_{rg} = 10$ V, denoted NN) or both sides p-doped ($V_{lg} = V_{rg} = -10$ V, denoted PP), the device shows a nearly ohmic current–voltage relation at low V_{ds} (Fig. 1b). The device has significantly higher conductance in NN, most probably due to the lower contact resistance between the gold and n-type WSe_2, as observed in MoS_2 (ref. 26). The current–voltage relations in these configurations are slightly nonlinear due to Schottky barriers, which we suspect dominate the contact resistance.

By oppositely biasing the two gates, the device rectifies current as a diode. Current measurements for the two diode configurations ($V_{lg} = -10$ V, $V_{rg} = 10$ V, denoted PN; $V_{lg} = 10$ V, $V_{rg} = -10$ V, denoted NP) are shown in Fig. 1b. At low V_{ds}, current in both PP and NN configurations is substantially larger than in NP and PN, demonstrating that the p–n junction dominates transport in this regime rather than Schottky barriers at the contacts. The effect of Schottky barriers is discussed further in the Supplementary Information. I_{ds} versus V_{ds} for PN and NP configurations

Department of Physics, Massachusetts Institute of Technology, 77 Massachusetts Avenue, Cambridge, Massachusetts 02139, USA, †These authors contributed equally to this work. *e-mail: pjarillo@mit.edu

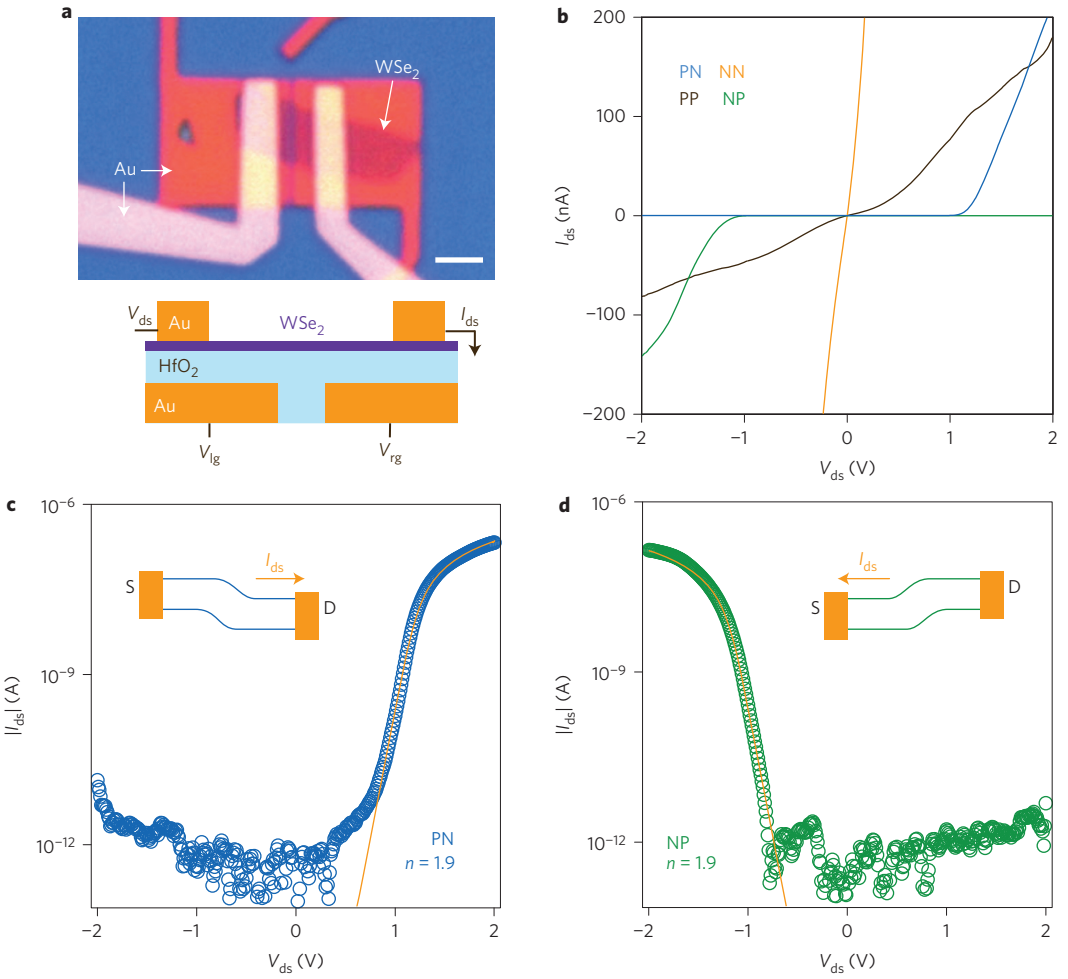

Figure 1 | Gate-controlled monolayer WSe_2 p–n junction diodes. a, Top: Optical micrograph of a monolayer WSe_2 device controlled by two local gates. The WSe_2 is contacted with gold electrodes. The flake and contacts are insulated from the gates by 20 nm HfO_2. Scale bar, 2 μm. Bottom: schematic side view of the device including electrical connections. **b**, Current-voltage (I_{ds}–V_{ds}) curves showing transport characteristics of four doping configurations of the device: NN, PP, PN and NP. Both gates were set to 10 V for the NN configuration and -10 V for PP. V_{lg} was set to ±10 V and V_{rg} to ∓ 10 V for PN/NP. The NN and PP configurations (yellow and black curves, respectively) are ohmic at low V_{ds}, while the PN and NP configurations (blue and green curves, respectively) strongly rectify current in opposite directions. **c**,**d**, Semi-logarithmic plots of I_{ds} through the PN (blue circles) and NP (green circles) diodes as a function of V_{ds}, with fits in yellow (see text). The fits give a diode ideality of $n = 1.9$ for both the PN and NP configurations. Insets: Schematic band diagrams of the device in forward bias for PN and NP configurations.

(Fig. 1c,d) is fit to the Shockley diode equation[27], extended[28] to include a series resistance, R_s:

$$I_{ds} = \frac{nV_T}{R_s} W\left[\frac{I_0 R_s}{nV_T}\exp\left(\frac{V_{ds} + I_0 R_s}{nV_T}\right)\right] - I_0$$

with $V_T = k_B T/q$ the thermal voltage at temperature T, k_B the Boltzmann constant, and q the electron charge. I_0 is the reverse-bias current and n is the diode ideality factor ($n = 1$ is ideal). W is the Lambert W function.

The rapid increase in current under forward bias defines an ideality factor of $n = 1.9$ for both PN and NP configurations, indicating that the current is mostly limited by recombination rather than diffusion[28]. Investigating this recombination, including contributions from Shockley–Read–Hall or Auger processes, will be a focus of future work. The roll-off of I_{ds} at high bias constrains $R_s = 3\ \mathrm{M\Omega}$ for PN and $R_s = 5\ \mathrm{M\Omega}$ for NP due to contact resistances. Environmental conditions such as substrate and fabrication residue most likely determine the contact resistance and the asymmetry between the PN and NP configurations. An increase in current at high reverse bias indicates a 0.5 TΩ shunt resistance across the junction. This large shunt resistance indicates a high-quality p–n interface and is an expected advantage of a lateral device geometry. Although our data do not strongly constrain the value of I_0, because it is below the 1 pA noise floor of the measurement, uncertainty in I_0 has an insignificant effect on the fits to the slope and roll-off of the current, and does not impact the values of n and R_s. Both diodes have rectification factors of 10^5 and reverse bias currents of <1 pA up to $|V_{ds}| = 1$ V, representing promising characteristics for low-power electronics.

A more complete view of transport through the device is shown in a map of current as a function of V_{lg} and V_{rg} (Fig. 2). The four corners of the map show the extremes of the four doping configurations (NN, PP, PN and NP). The off state of the device can be seen in the dark blue region in the centre of the map, separating the four conducting regions. Although mid-gap states, most likely due to disorder, form a conducting region between the NN and NP quadrants, current through these states is thermally activated and can be eliminated by cooling the device (Supplementary Fig. 3).

Along the diagonal line defined by $V_{bg} = V_{lg} = V_{rg}$, line cuts show the device operating as an ambipolar field-effect transistor

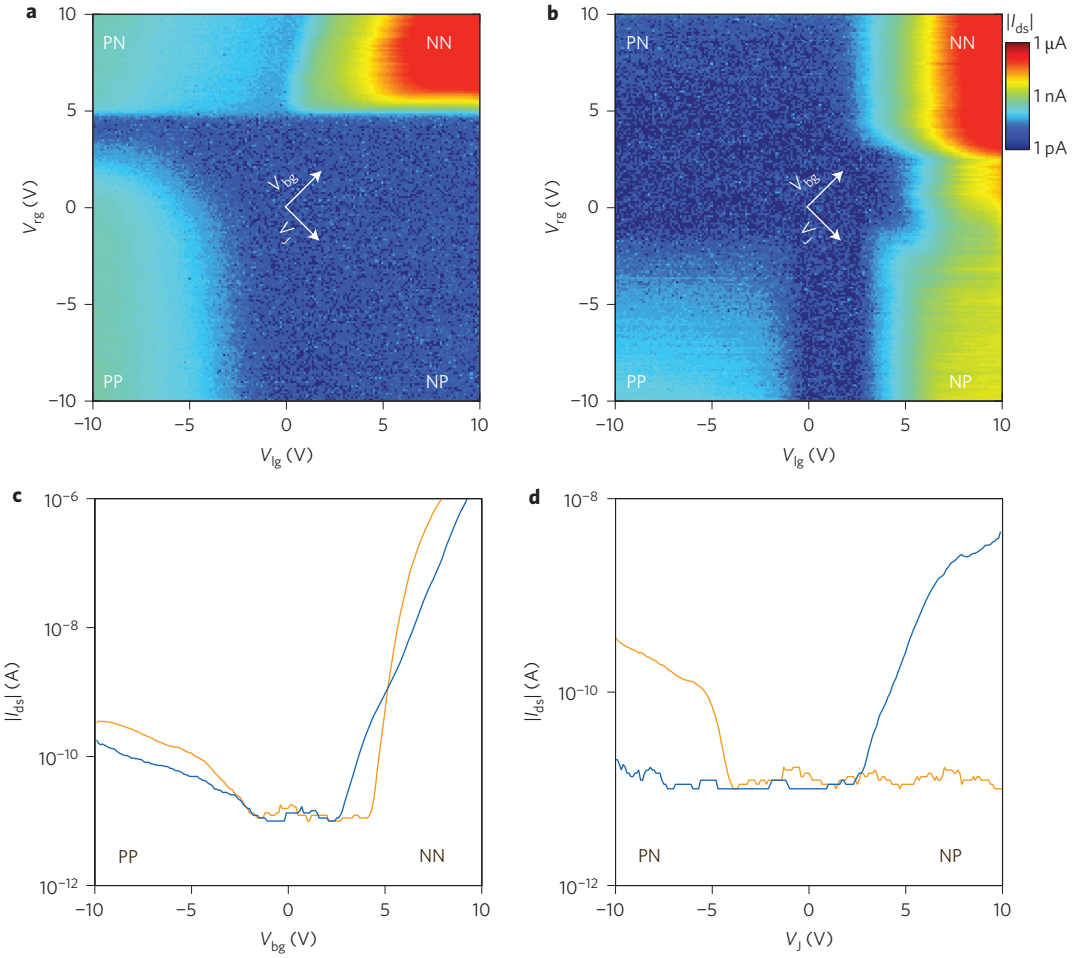

Figure 2 | Current through the device as a function of doping configuration. a,**b**, Current magnitude through the device, $|I_{ds}|$, as the drain source bias V_{ds} is held at 2 V (**a**) and -2 V (**b**) and the two backgates are varied independently. The colour scale is logarithmic from 1 pA to 1 μA. **c**, Diagonal cuts of $|I_{ds}|$ where both gates are swept together as one backgate, $V_{bg} = V_{lg} = V_{rg}$, for $V_{ds} = 2$ V (yellow curve) and -2 V (blue curve). These curves are characteristic of an ambipolar field-effect transistor. **d**, Off-diagonal cuts of $|I_{ds}|$ where the two gates are swept with opposite polarity, showing the dependence of the current on the asymmetric gate voltage, $V_J = V_{lg} = -V_{rg}$, which defines the junction. The current was measured at $V_{ds} = 2$ V (yellow curve) and -2 V (blue curve), demonstrating rectification of current in opposite directions for p-n ($V_J < 0$) and n-p ($V_J > 0$) gate configurations.

(Fig. 2c). Along the off-diagonal, line cuts show gate-controlled rectifying behaviour (Fig. 2d) as a function of the asymmetric gate voltage, $V_J = V_{lg} = -V_{rg}$, which defines a junction between the p- and n-type regions. We note a decrease in device performance between the data sets presented in Fig. 1 and Fig. 2. We suspect that this decrease stems from local Joule heating at the contacts when the device is operated at high V_{ds}.

The optoelectronic properties of monolayer WSe_2 p–n diodes were investigated with scanning photocurrent microscopy (Fig. 3a), where I_{ds} is measured as a laser spot (~2 μm diameter) is scanned over the sample. With the gates in the NP configuration, photons impinging on the junction create electron–hole pairs, which are separated to opposite contacts by the electric field at the junction, generating a photocurrent. Scanning the beam (power 75 μW, wavelength 830 nm) over the sample and measuring I_{ds} at $V_{ds} = 0$ yields a spatial map of the photoresponse of the device (Fig. 3b). Calibrating the photocurrent map with a simultaneously acquired image of reflected light from the sample (Supplementary Fig. 4), we overlaid the positions of the contacts and gates to demonstrate that maximum photocurrent arises when light is incident on the junction. A line cut through the centre of the photocurrent map is shown in Fig. 3c with the positions of the contacts and the junction illustrated for reference. The photocurrent is symmetric and centred on the junction, demonstrating that the photoresponse is dominated by the p–n junction and not Schottky barriers at the contacts (Supplementary Fig. 3).

At relatively large V_{ds} in the NP configuration, a substantial photocurrent is generated when the junction is illuminated with laser light at 532 nm. The I_{ds}–V_{ds} curves at laser powers of 0–10 μW are shown in Fig. 3d. The photocurrent $I_{ph} = I_{ds,light} - I_{ds,dark}$ at $V_{ds} = -2$ V and a linear fit of I_{ph} up to 8 μW are shown in the inset. The slope from the fit gives a responsivity of 210 mA W^{-1}, which is comparable to commercial silicon photodetectors for green light. We note that phototransistors based on monolayer dichalcogenides can achieve even higher responsivities[16], although the principle of operation and device geometry differ significantly from the photodiodes presented here.

In addition to photodetection, monolayer WSe_2 p–n diodes are also capable of photovoltaic power generation. With the device in the NP configuration, current is measured as a function of V_{ds} for various laser powers from a supercontinuum white-light source bandpass filtered at 700 nm. Figure 4a presents a zoomed-in view of the I_{ds}–V_{ds} curve, focusing on the quadrant of photovoltaic power generation. The short-circuit current I_{sc}, which is the zero-bias current through the illuminated device, increases linearly with power up to at least 10 μW (Fig. 4a, inset). The power generated by the photovoltaic device, $P = I_{ds}V_{ds}$, is shown for laser

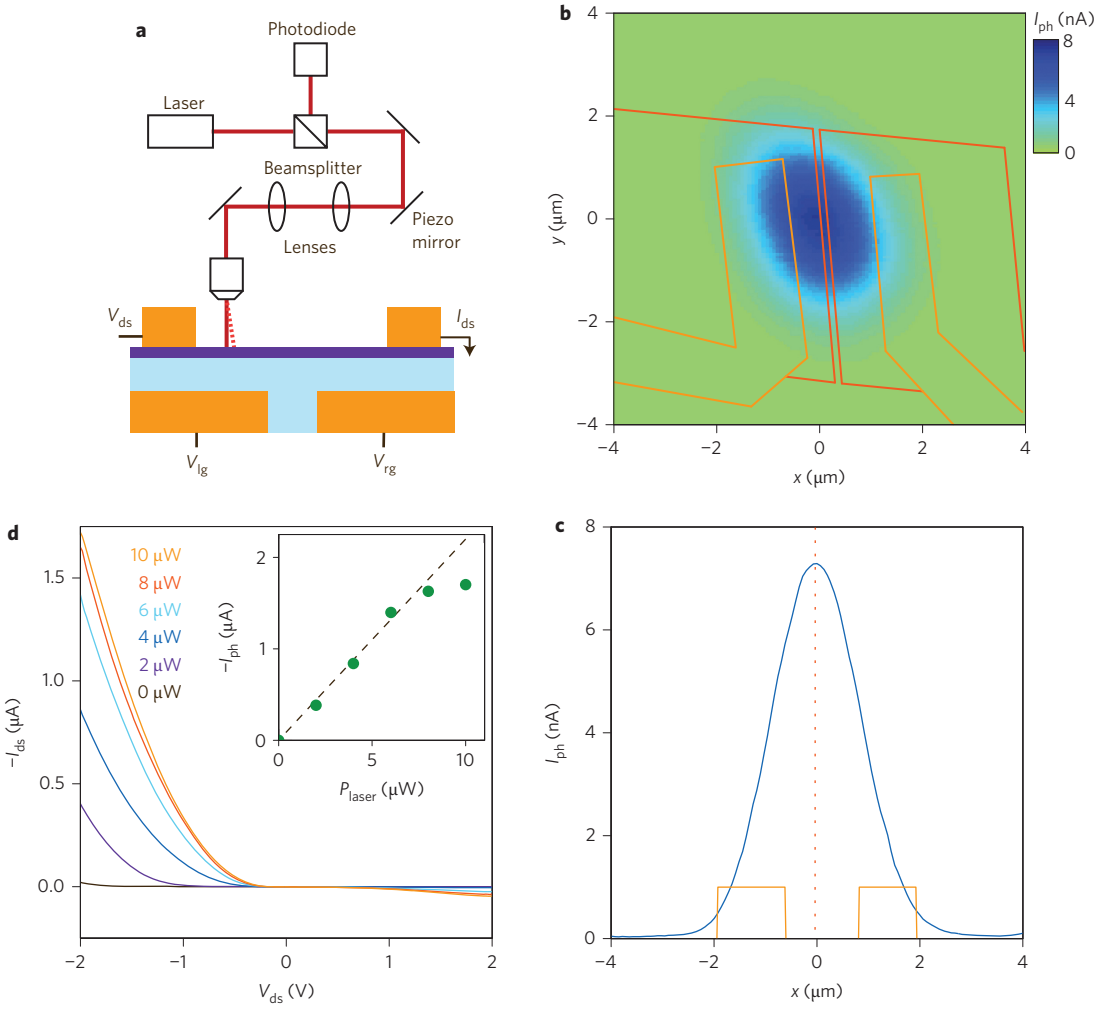

Figure 3 | Photodetection in monolayer WSe_2. **a**, Schematic of scanning photocurrent microscopy set-up and the device. The laser (solid red line) is focused onto the sample through a microscope objective at a position set by a piezo-controlled mirror. As the laser is scanned over the sample (represented by the dashed red line), photocurrent is recorded simultaneously with the reflected laser power measured by a photodiode. **b**, Photocurrent I_{ph} as a function of laser position (75 μW, 830 nm diode laser), with the device in the NP configuration and $V_{ds} = 0$ V. The peak in current corresponds to the location of the junction. Outlines of the contacts (orange lines) and gates (red lines) are overlaid on the current map based on the reflected image (Supplementary Fig. 4). **c**, Line cut from **b** at $y = 0$ (blue curve). Outlines of the contacts (orange rectangles) and the position of the junction (red dotted line) are shown based on the reflected image. **d**, I_{ds}–V_{ds} characteristics with the device in the NP configuration at laser powers of 0–10 μW from a 532 nm diode laser. Inset: I_{ph} (green dots) at $V_{ds} = -2$ V as a function of laser power. A linear fit (black dashed line) to I_{ph} for powers 0–8 μW gives a responsivity of 210 mA W^{-1}.

powers of 0–10 μW in Fig. 4b. The photovoltaic power generation also has a linear dependence on laser power (Supplementary Fig. 5).

Varying V_J, the asymmetric gate voltage that defines the junction, at different laser powers, we observe a saturation in the short-circuit current when $V_J \approx \pm 5$ V (Fig. 4c). The current is higher for NP than for PN due to a difference in contact resistances between the two contacts. We also note that the photocurrent due to the photovoltaic effect in these WSe_2 diodes is approximately an order of magnitude larger than photothermoelectric currents observed at the contacts of a monolayer MoS_2 field-effect transistor[29].

To obtain spectrally resolved photocurrent in the NP configuration, we measure I_{sc} as a function of excitation wavelength. To quantify the efficiency of light conversion into current, we extract the external quantum efficiency, EQE$= (I_{sc}/P_{laser})(hc/e\lambda)$, as a function of wavelength λ, at constant laser power P_{laser}, where h, c and e are Planck's constant, the speed of light and electron charge, respectively. We observe three peaks in the spectrally resolved photocurrent at 755, 591 and 522 nm (Fig. 4d), corresponding to energies of 1.64, 2.10 and 2.38 eV, respectively. These energies match well with the values observed via photoluminescence[8], differential reflectance[19] and optical absorption spectroscopy[30] for the A, B and A′ transitions of monolayer WSe_2, as depicted in the band diagram in the inset to Fig. 4d. We measure a maximum EQE of 0.2% at 522 nm. This value does not take into account the low absorption of monolayer WSe_2 or the narrow cross-section of the p–n junction relative to the size of the laser spot, which together suggest an internal quantum efficiency at least an order of magnitude larger than the EQE reported here.

Finally, we measure the electroluminescence spectrum of a second monolayer WSe_2 p–n diode (Fig. 4d). To improve hole injection, this device was fabricated with palladium instead of gold to contact the p-type WSe_2 (Supplementary Fig. 2). In the PN configuration ($V_{ds} = 2$ V, $I_{ds} = 100$ nA), the device behaves as a light-emitting diode. The emitted light spectrum peaks at 752 nm, corresponding to the direct-gap exciton transition seen in the photocurrent spectrum (Fig. 4d). Using a blackbody source for calibration, we estimate the electroluminescence efficiency, defined as optical output power divided by electrical input power, to be ~1%. Light emission and a peak at ~750 nm are also seen in the NP configuration ($V_{ds} = -2$ V, $I_{ds} = 4$ nA), with a peak height smaller in

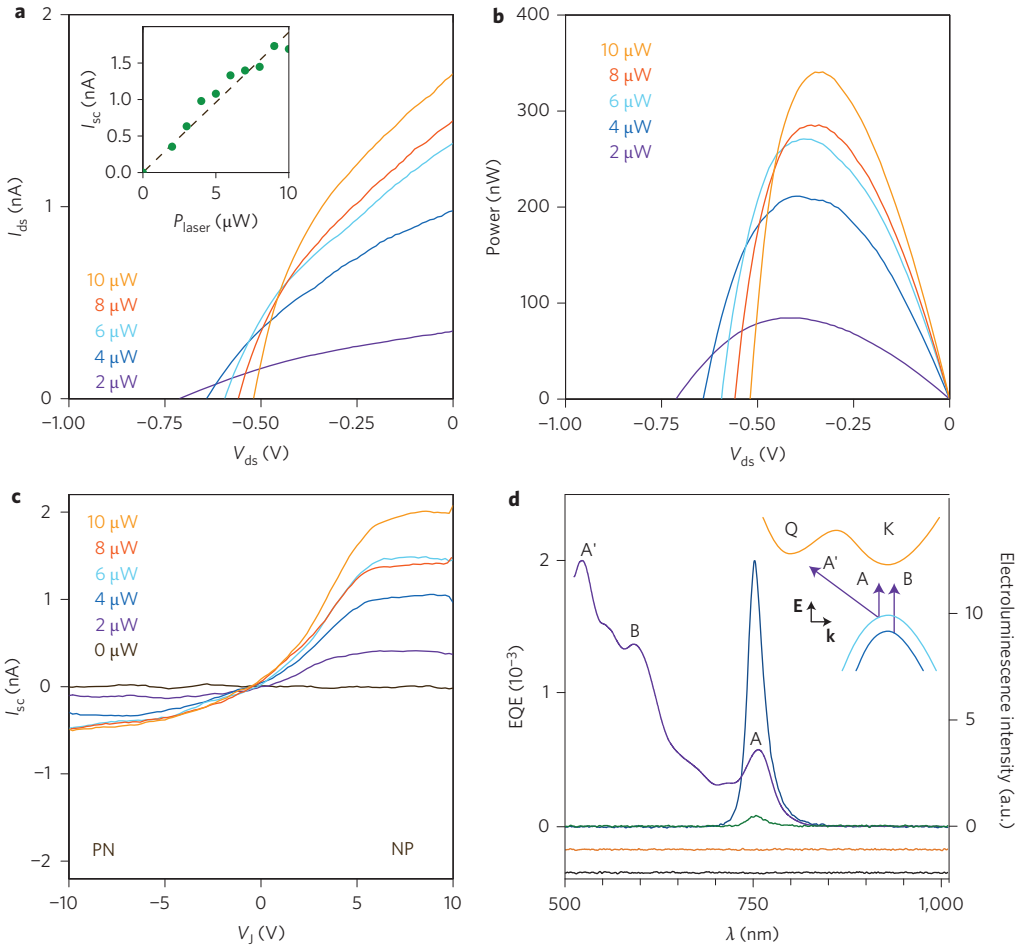

Figure 4 | Photovoltaic response and light emission. a, I_{ds} as a function of V_{ds} in the NP configuration for laser powers 2–10 μW (wavelength 700 nm). Positive I_{ds} and negative V_{ds} in this regime reflects photovoltaic power generation. Inset: Short-circuit current I_{sc} (green dots) versus laser power with a linear fit (black dashed line). **b**, Power $P = I_{ds}V_{ds}$ produced by the device as a function of V_{ds} for different incident laser powers, calculated from the data in **a**. **c**, I_{sc} as a function of asymmetric gate voltage, V_J, for different laser powers. I_{sc} is nearly linear with power up to 10 μW in the NP configuration, although it saturates in the PN configuration beyond 6 μW. As a function of gate voltage, the current saturates in both configurations for $V_J = \pm 5$ V. **d**, Left axis: EQE as a function of wavelength at a constant laser power of 2 μW in the NP configuration (purple line). Peaks in the EQE correspond to exciton transitions A, B and A′, as labelled. Right axis: electroluminescence intensity from a second monolayer WSe_2 device with one gold and one palladium contact. $V_{ds} = 2$ V in the PN (blue trace), NN (yellow trace) and PP (black trace) configurations, and $V_{ds} = -2$ V in the NP (green trace) configuration. NN and PP traces are offset vertically for clarity. Inset: Diagram of the band structure around the K and Q points, with arrows indicating the lowest-energy exciton transitions for monolayer WSe_2.

proportion to I_{ds}. No emission is seen in either NN (with $V_{ds} = 2$ V and $I_{ds} = 300$ nA) or PP (with $V_{ds} = 2$ V and $I_{ds} = 500$ nA) configurations, confirming that the gate-defined p–n junction generates the electroluminescence. A spatial image of light emission from a third device is shown in Supplementary Fig. 6.

Based on the device performance presented here, we anticipate a prominent role for diodes and optoelectronic devices based on monolayer dichalcogenide p–n junctions. Taking into account the three-atom thickness and low optical absorption of monolayer WSe_2 (ref. 30), the responsivity and EQE reported here are quite substantial. Furthermore, the device geometry could be optimized to significantly enhance the photoresponse. We expect that vertical junctions based on transfer-aligned exfoliated flakes[25] or large-area dichalcogenides grown by chemical vapour deposition[30] could increase responsivity and EQE by more than an order of magnitude. Additionally, improved contact resistance, particularly for holes, should dramatically improve device performance.

In conclusion, we have demonstrated electrically tunable p–n diodes based solely on monolayer WSe_2. These diodes strongly rectify current, in a direction selectable by the two gates controlling the device. Both PN and NP configurations have diode ideality factors of $n = 1.9$ and a rectification factor of 10^5. With laser light incident on the junction, these diodes produce a large photocurrent with a responsivity of 210 mA W^{-1} at high bias. At low bias, the diodes generate power via the photovoltaic effect, with a peak EQE of 0.2% at 522 nm. The spectral response of the photocurrent from visible to near-infrared wavelengths showed peaks corresponding to the three lowest excitonic transitions expected for monolayer WSe_2. Finally, these devices also function as light-emitting diodes with an electroluminescence peak at 752 nm. These p–n diodes demonstrate the potential of monolayer WSe_2, in addition to other direct-gap semiconducting dichalcogenides, for novel electronic and optoelectronic applications. As device quality improves, they also lay the foundation for more fundamental quantum transport experiments[31].

Note added in proof: During the preparation of this Letter we became aware of two similar studies[32,33].

Methods

Device fabrication began with exfoliation of bulk, natural WSe_2 (Nanosurf) down to few-layered sheets using the mechanical cleavage method pioneered for graphene. The thin flakes were deposited onto a transfer slide composed of a stack of glass, a polymer (polydimethylsiloxane, PDMS) and a resist (methyl methacrylate, MMA),

as described for graphene–boron nitride device fabrication[25]. Single molecular layers were identified by optical contrast. Layer number was later confirmed using atomic force microscopy and either photocurrent spectroscopy or electroluminescence (Supplementary Section 'Device Fabrication'). The monolayers were transferred onto a pair of split gates covered by 20 nm HfO_2 (grown by atomic layer deposition at 80°C). The gates were separated by a 100 nm gap, patterned using electron-beam lithography on a highly doped silicon substrate covered in 285 nm thermally grown SiO_2. The gates were made from electron-beam evaporated gold and were 20 nm thick. The two backgates were capacitively coupled to the device through the HfO_2 dielectric, which has a dielectric constant, $\epsilon_r \approx 15$. The WSe_2 was contacted by two gold electrodes, each ~1 μm wide and 25 nm thick, with a 0.3 nm chromium sticking layer.

All measurements were performed at room temperature and in vacuum ($\sim 10^{-5}$ torr) to avoid device degradation from adsorbates present in air, which could be mitigated by encapsulation of the WSe_2. Electroluminescence was measured using a liquid nitrogen-cooled charged-coupled device with an integration time of 60 s. A background measured at $V_{ds} = 0$ was subtracted from all four electroluminescence traces in Fig. 4d.

Received 2 October 2013; accepted 21 January 2014; published online 9 March 2014

References

1. Martel, R. *et al.* Ambipolar electrical transport in semiconducting single-wall carbon nanotubes. *Phys. Rev.Lett.* **87,** 256805 (2001).
2. Koo, S.-M., Li, Q., Edelstein, M., Richter, C. & Vogel, E. Enhanced channel modulation in dual-gated silicon nanowire transistors. *Nano Lett.* **5,** 2519–2523 (2005).
3. Zaumseil, J. & Sirringhaus, H. Electron and ambipolar transport in organic field-effect transistors. *Chem. Rev.* **107,** 1296–1323 (2007).
4. Bertolazzi, S., Brivio, J. & Kis, A. Stretching and breaking of ultrathin MoS_2. *ACS Nano* **5,** 9703–9709 (2011).
5. Mak, K. F., Lee, C., Hone, J., Shan, J. & Heinz, T. F. Atomically thin MoS_2: a new direct-gap semiconductor. *Phys. Rev. Lett.* **105,** 136805 (2010).
6. Chuang, S. *et al.* Near-ideal electrical properties of InAs/WSe_2 van der Waals heterojunction diodes. *Appl. Phys. Lett.* **102,** 242101 (2013).
7. Tonndorf, P. *et al.* Photoluminescence emission and Raman response of monolayer MoS_2, $MoSe_2$, and WSe_2. *Opt. Express* **21,** 4908–4916 (2013).
8. Zhao, W. *et al.* Evolution of electronic structure in atomically thin sheets of WS_2 and WSe_2. *ACS Nano* **7,** 791–797 (2013).
9. Geim, A. K. & Grigorieva, I. V. Van der Waals heterostructures. *Nature* **499,** 419–425 (2013).
10. Wilson, J. & Yoffe, A. The transition metal dichalcogenides discussion and interpretation of the observed optical, electrical and structural properties. *Adv. Phys.* **18,** 193–335 (1969).
11. Podzorov, V., Gershenson, M. E., Kloc, C., Zeis, R. & Bucher, E. High-mobility field-effect transistors based on transition metal dichalcogenides. *Appl. Phys. Lett.* **84,** 3301–3303 (2004).
12. Radisavljevic, B. & Kis, A. Mobility engineering and a metal–insulator transition in monolayer MoS_2. *Nature Mater.* **12,** 815–820 (2013).
13. Zhang, Y. J., Ye, J. T., Yomogida, Y., Takenobu, T. & Iwasa, Y. Formation of a stable p–n junction in a liquid-gated MoS_2 ambipolar transistor. *Nano Lett.* **13,** 3023–3028 (2013).
14. Wang, H. *et al.* Integrated circuits based on bilayer MoS_2 transistors. *Nano Lett.* **12,** 4674–4680 (2012).
15. Yin, Z. *et al.* Single-layer MoS_2 phototransistors. *ACS Nano* **6,** 74–80 (2012).
16. Lopez-Sanchez, O., Lembke, D., Kayci, M., Radenovic, A. & Kis, A. Ultrasensitive photodetectors based on monolayer MoS_2. *Nature Nanotech.* **8,** 497–501 (2013).
17. Sundaram, R. S. *et al.* Electroluminescence in single layer MoS_2. *Nano Lett.* **13,** 1416–1421 (2013).
18. Ye, Y. *et al.* Exciton-related electroluminescence from monolayer MoS_2. Preprint at http://lanl.arXiv.org/abs/1305.4235 (2013).
19. Zeng, H. *et al.* Optical signature of symmetry variations and spin-valley coupling in atomically thin tungsten dichalcogenides. *Sci. Rep.* **3,** 1608 (2013).
20. Mak, K. F., He, K., Shan, J. & Heinz, T. F. Control of valley polarization in monolayer MoS_2 by optical helicity. *Nature Nanotech.* **7,** 494–498 (2012).
21. Sallen, G. *et al.* Robust optical emission polarization in MoS_2 monolayers through selective valley excitation. *Phys. Rev. B* **86,** 081301 (2012).
22. Jones, A. M. *et al.* Optical generation of excitonic valley coherence in monolayer WSe_2. *Nature Nanotech.* **8,** 634–638 (2013).
23. Spah, R., Elrod, U., Luxsteiner, M., Bucher, E. & Wagner, S. PN junctions in tungsten diselenide. *Appl. Phys. Lett.* **43,** 79–81 (1983).
24. Lee, J. U., Gipp, P. P. & Heller, C. M. Carbon nanotube p–n junction diodes. *Appl. Phys. Lett.* **85,** 145–147 (2004).
25. Dean, C. R. *et al.* Boron nitride substrates for high-quality graphene electronics. *Nature Nanotech.* **5,** 722–726 (2010).
26. Radisavljevic, B., Radenovic, A., Brivio, J., Giacometti, V. & Kis, A. Single-layer MoS_2 transistors. *Nature Nanotech.* **6,** 147–150 (2011).
27. Sah, C.-T., Noyce, R. N. & Shockley, W. Carrier generation and recombination in p–n junctions and p–n junction characteristics. *Proc. IRE* **45,** 1228–1243 (1957).
28. Banwell, T. & Jayakumar, A. Exact analytical solution for current flow through diode with series resistance. *Electron. Lett.* **36,** 291–292 (2000).
29. Buscema, M. *et al.* Large and tunable photo-thermoelectric effect in single-layer MoS_2. *Nano Lett.* **13,** 358–363 (2013).
30. Huang, J.-K. *et al.* Large-area and highly crystalline WSe_2 monolayers: from synthesis to device applications. *ACS Nano* **8,** 923–930 (2014).
31. Li, X., Zhang, F. & Niu, Q. Unconventional quantum Hall effect and tunable spin Hall effect in Dirac materials: application to an isolated MoS_2 trilayer. *Phys. Rev. Lett.* **110,** 066803 (2013).
32. Pospischil, A., Furchi, M. M. & Mueller, T. Solar-energy conversion and light emission in an atomic monolayer p–n diode. *Nature Nanotech.* http://dx.doi.org/10.1038/nnano.2014.14 (2014).
33. Ross, J. *et al.* Electrically tunable excitonic light-emitting diodes based on monolayer WSe_2 p–n junctions. *Nature Nanotech.* http://dx.doi.org/10.1038/nnano.2014.26 (2014).

Acknowledgements

The authors are grateful for experimental assistance provided by K. Akkaravarawong, T. Andersen, N. Gabor, Q. Lin, Q. Ma, W. Fang and J. Sanchez-Yamagishi, as well as for discussions with P. Brown. This work was primarily funded by the Office of Naval Research Young Investigator Award (N00014-13-1-0610) and partly by the Office of Naval Research Graphene Approaches to Terahertz Electronics Multidisciplinary University Research Initiative and a Packard Fellowship. This work made use of the Materials Research Science and Engineering Center Shared Experimental Facilities supported by the National Science Foundation (NSF) (award no. DMR-0819762) and of Harvard's Center for Nanoscale Systems, supported by the NSF (grant ECS-0335765).

Author contributions

B.W.H.B., H.O.H.C. and Y.Y. fabricated the samples. B.W.H.B., H.O.H.C. and Y.Y. performed the measurements. All authors analysed the data and co-wrote the paper.

Additional information

Supplementary information is available in the online version of the paper. Reprints and permissions information is available online at www.nature.com/reprints. Correspondence and requests for materials should be addressed to P.J.H.

Competing financial interests

The authors declare no competing financial interests.